The Astrophysical Journal, 893:69 (8pp), 2020 April 10 https://doi.org/10.3847/1538-4357/ab7db7

Subaru Medium-resolution Spectra of a QSO at $z = 6.62$: Three Reionization Tests

Ting-Yi Lu[1], Tomotsugu Goto[1], Ji-Jia Tang[2,3,4], Tetsuya Hashimoto[1,5], Yi-Hang Valerie Wong[1], Chia-Ying Chiang[1], Yi-Han Wu[1], Seong Jin Kim[1], Simon C.-C. Ho[1], Ting-Wen Wang[1], Alvina Y. L. On[1,5,6], and Daryl Joe D. Santos[1]
[1] Institute of Astronomy, National Tsing Hua University, 101, Sec. 2, Kuang Fu Rd., Hsinchu 30013, Taiwan; tingyilu@gapp.nthu.edu.tw
[2] Research School of Astronomy and Astrophysics, Australian National University, Cotter Road, Weston Creek, ACT 2611, Australia
[3] Graduate Institute of Astrophysics, National Taiwan University, No.1 Sec. 4 Roosevelt Rd., Taipei 10617, Taiwan
[4] Institute of Astronomy and Astrophysics, Academia Sinica, No.1, Sec. 4, Roosevelt Rd., Taipei 10617, Taiwan
[5] Centre for Informatics and Computation in Astronomy, National Tsing Hua University, 101, Section 2. Kuang-Fu Road, Hsinchu, 30013, Taiwan
[6] Mullard Space Science Laboratory, University College London, Holmbury St Mary, Surrey RH5 6NT, UK
Received 2019 October 30; revised 2020 February 26; accepted 2020 March 6; published 2020 April 16

Abstract

Investigating the Gunn–Peterson (GP) trough of high-redshift quasars (QSOs) is a powerful way to reveal the cosmic reionization. As one of such attempts, we perform a series of analyses to examine the absorption lines observed with one of the highest-redshift QSOs, PSO J006.1240+39.2219, which we previously discovered at $z = 6.62$. Using the Subaru telescope, we obtained medium-resolution spectrum with a total exposure time of 7.5 hr. We calculate the Lyα transmission in different redshift bins to determine the near zone radius and the optical depth at $5.6 < z < 6.5$. We find a sudden change in the Lyα transmission at $5.75 < z < 5.86$, which is consistent with the result from the literature. The near zone radius of the QSO is 5.79 ± 0.09 *p*Mpc, within the scatter of the near zone radii of other QSOs measured in previous studies. We also analyze the dark gap distribution to probe the neutral hydrogen fractions beyond the saturation limit of the GP trough. We extend the measurement of the dark gaps to $5.7 < z < 6.3$. We find that the gap widths increase with increasing redshifts, suggesting more neutral universe at higher redshifts. However, these measurements strongly depend on the continuum modeling. As a continuum model-free attempt, we also perform the dark pixel counting analysis to find the upper limit of $\langle x_{\rm H\,I}\rangle \sim 0.6$ (0.8) at $z < 5.8$ ($z > 5.8$). All three analyses based on this QSO show increasingly neutral hydrogen toward higher redshifts, adding precious measurements up to $z \sim 6.5$.

Unified Astronomy Thesaurus concepts: Reionization (1383); Early universe (435); Quasars (1319); Quasar absorption line spectroscopy (1317); Observational cosmology (1146); Intergalactic medium (813); Intergalactic medium phases (814)

1. Introduction

Cosmic reionization is a major phase change of the universe when the neutral intergalactic medium (IGM) was being ionized by the ultraviolet (UV) radiation from the first luminous objects (Barkana & Loeb 2001; Loeb & Barkana 2001; Fan et al. 2006a). It is crucial to uncover the reionization history and the early evolution of the ionizing sources. To date, the mid-point of the reionization has been constrained to be at $z = 7.7 \pm 0.7$ from the cosmic microwave background observation by Planck Collaboration et al. (2018). High-redshift quasars (QSOs) have been used as probes for the end of the reionization (see Mortlock 2016 for a review). By measuring the Lyα transmissions at different redshifts in the UV continuum of a QSO, and therefore the Gunn–Peterson (GP) optical depths, the end of the reionization at that line of sight (LOS) can be revealed. Previously, the occurrences of the GP troughs (where the Lyα absorptions in the spectra of QSOs are saturated) through different LOSs have been reported to be at $z \sim 6$ (e.g., Becker et al. 2001, 2015; Songaila 2004; Fan et al. 2006b; Bolton et al. 2011; Goto et al. 2011; Eilers et al. 2017, 2018; Bosman et al. 2018), indicating the end stage of the reionization. On the other hand, because the GP optical depth is very sensitive to the fractional change of the scarcely remaining neutral hydrogen (neutral fraction, $x_{\rm H\,I} \sim 10^{-4}$) during that stage (Gunn & Peterson 1965; Fan et al. 2006a), the occurrence of the GP trough limits our capability in probing the end stage of the reionization toward $z \gtrsim 6$, where the average $x_{\rm H\,I}$ becomes higher than 10^{-4}. In addition, current simulations (Keating et al. 2019, 2020; Nasir & D'Aloisio 2019) suggest that the scatter of GP optical depth (Fan et al. 2006b; Becker et al. 2015; Bosman et al. 2018; Eilers et al. 2018) could be explained by late reionization model as well. Thus, to advance the research, other analyses on the $z \gtrsim 6$ QSOs are required.

One of the alternative, higher order approaches to measure reionization at high redshift is to measure the frequency of high Lyα transmission peaks in the spectra (Croft & Gaztañaga 1998; Songaila & Cowie 2002). Such transmission peaks can trace the higher ionization state regions in the GP trough. The practical measurement on the frequency is performed by counting the dark gaps, which is the gap constructed by two adjacent peaks. Songaila & Cowie (2002) first illustrated the distribution of the dark gap in QSO spectra at $3.5 < z < 5.5$ using a sample of 15 QSOs at $4.42 \leqslant z \leqslant 5.75$. Paschos & Norman (2005) generated the synthetic spectra of the Lyα forest up to $z \sim 6.6$ and performed the simulation of the dark gap distribution in the spectra at $z = 5.5$–6.0 and $z = 6.0$–6.5. Gallerani et al. (2006) performed the dark gap simulation at similar redshift with larger box size. Then Fan et al. (2006b) extended the dark gap measurement to $z \sim 6$ with a sample of 19 QSOs. These studies suggested that the gap width may have a notable change at $z \sim 6$. More recently, Gnedin et al. (2017) present the comparison between the simulations from the Cosmic Reionization On Computers project and the observations of the QSOs at $5.7 < z < 6.4$ from Fan et al. (2006b) and Becker et al. (2015). The shape of the transmission peaks may also be a sensitive probe of the IGM environment. In addition to the above two methods that are dependent on the assumption

Table 1
Properties of PSO J006.1240+39.2219

Object	R.A. (J2000)	Decl. (J2000)	$z_{\rm [C\,II]}$	$R_{\rm p,NZ}$ (pMpc)	$R_{\rm NZ,cor}$ (pMpc)
PSO J006.1240+39.2219	00:24:29.657	+39:12:00.66	6.621 ± 0.002[a]	4.19 ± 0.06	5.79 ± 0.09

Note.
[a] Mazzucchelli et al. (2017).

of intrinsic UV continuum, McGreer et al. (2011) provided a model-free constraint on the upper limit of the volume-averaged neutral fraction by counting the covering fraction of dark pixels, which are the pixels with no flux detected. However, these analyses are more demanding on the signal-to-noise ratio (S/N) of the data to minimize the impact of the noise on the low transmission region.

So far, ∼50 QSOs at $z > 6.5$ have been discovered (see Inayoshi et al. 2019 for a full list of the 203 known $z > 6$ QSOs). While only $\lesssim$10 of them are used to constrain the reionization (Tang et al. 2017; Bañados et al. 2018; Bosman et al. 2018; Eilers et al. 2018) due to the expensiveness of obtaining high quality spectra. To push the constraint to $z \gtrsim 6.5$ statistically, more sight lines through the corresponding redshift should be observed.

In this paper, we carry out a follow-up investigation on PSO J006.1240+39.2219 ($z = 6.621$) with the Subaru Faint Object Camera and Spectrograph (FOCAS; Kashikawa et al. 2002). We observe the medium-resolution UV spectrum of this QSO in order to add a sight line to the $z \gtrsim 6.5$ sample to constrain reionization at high redshift. In addition, since this QSO is a super-Eddington QSO (Tang et al. 2019), it is of interest to study its physical properties via emission lines. We present the line luminosities in Section 3. The IGM transmission, the GP optical depth, and the near zone radius of this QSO, which will help constraining the IGM neutral fraction, are presented in Section 3.1. Furthermore, as we take advantage of the high S/N optical spectrum, we are able to perform dark gap statistics to investigate the subtle change of the structure in the spectrum (Section 3.2) and the dark pixel test, which is a nearly model-independent measurement of the volume-averaged neutral fraction (Section 3.3), for the first time to $z \sim 6.5$.

Throughout the paper, we use a ΛCDM cosmology with $H_0 = 70$ km s^{-1} Mpc^{-1}, $\Omega_m = 0.3$, and $\Omega_\Lambda = 0.7$.

2. Data

In previous work, we discovered PSO J006.1240+39.2219 (Tang et al. 2017), yet the spectrum was of low resolution and a short exposure time of 5000 s and the S/N at 1250 Å $< \lambda_{\rm rest} <$ 1280 Å was only 9.82. Therefore, we carry out an additional spectroscopic observation of PSO J006.1240 +39.2219 with the Subaru/FOCAS using the medium-resolution VPH950 grism with a 058 blocking filter (PI: Goto). The exposure time is 27,000 s, or 7.5 hr. The wavelength coverage is from 7500 to 10450 Å. The spectral resolution with the 0.″4 slit is $R \sim 5500$. The information of this QSO is summarized in Table 1. We adopt the redshift calculated by Mazzucchelli et al. (2017) based on [C II] 158 μm line. The spectrum of the QSO we obtained is shown in Figure 1.

Data reduction is performed in a standard manner using IRAF. After flat-fielding, the wavelength calibration is performed using skylines. We perform first-order sky background subtraction using 60 pixels on both sides of the QSO position in the spatial direction. We chose the sky regions as close to the QSO as possible, but at the same time, avoiding the tail of the QSO flux. After subtracting the background, the 1σ clipped median flux blueward of the QSO's near zone region is $1.15 \pm 6.33 \times 10^{-19}$ erg cm^{-2} s^{-1} Å^{-1}, which is consistent with zero. The median S/N at 1250 Å $< \lambda_{\rm rest} <$ 1280 Å is 17.95. We observe BD+28D4211 as a standard star for 90 s. We apply the same trace as our standard star because the QSO flux blueward of Lyα is significantly absorbed. This star is used for flux calibration. The 1D extracted spectrum is then binned into ∼1.5 Å pixel^{-1}.

3. Analyses

For the analysis in the later sections, we use the power-law equation $F_\lambda = F_0\,(\lambda/2500\ \text{Å})^{\alpha_\lambda}$ (Mazzucchelli et al. 2017) to fit the continuum. We adopt the slope of $\alpha_\lambda = -2.94 \pm 0.03$ that is fitted to the rest-frame wavelength windows [1285–1295; 1315–1325; 1340–1375; 1425–1470; 1680–1710; 1975–2050; 2150–2250; and 2950–2990] Å of the near-infrared spectrum from Tang et al. (2019). The F_0 fitted to the wavelength window is $5.40 \pm 0.05 \times 10^{19}$ erg s^{-1} cm^{-2} Å^{-1}. The windows are selected to avoid the strong emission lines.

We also estimate the luminosity of the Lyα, N$_{\rm V}$, λ1239,1243, and O$_{\rm I}$ λ1304+ Si$_{\rm II}$ λ1306 emission lines by fitting double Gaussian plots. The results are shown in Figure 1 and Table 2.

3.1. IGM Optical Depth

To investigate neutral hydrogen absorption as a function of redshift, we follow various methods from previous studies (e.g., Fan et al. 2002; Songaila 2004; Becker et al. 2015; Tang et al. 2017; Bosman et al. 2018) to perform a GP test on the QSO with the fitted power-law continuum plus Lyα emission as the intrinsic flux. In this test, the steep rise of the average transmission can be considered to be a sign of the end of the reionization.

We measure the average transmission of the Lyα, the weighted Lyβ transmissions, and the optical depths at 7939–9139 Å (Lyα) and 7548–7732 Å (Lyβ). We select these wavelength intervals in order to avoid the Lyα emission line, the near zone region, and the Lyβ emission line. But the highest-redshift bin could be contaminated by the near zone. The wavelength range is divided into 50 cMpc h^{-1} bins. Aside from that, we masked the wavelengths with strong skyline residuals while measuring transmission.

The Lyα transmission (T) is measured as $T = \langle F_{\nu,\rm obs}/F_{\nu,\rm int}\rangle$, and the optical depths (τ) are derived from the transmissions, where $\tau = -\ln(T)$ (Fan et al. 2006b). $F_{\nu,\rm obs}$ is the observed flux and $F_{\nu,\rm int}$ is the intrinsic continuum. Our transmission spectrum and the transmission spectrum from Tang et al. (2017) are shown in Figure 2 for comparison. Since the Lyβ forest overlaps with the Lyα forest in the spectrum, and the Lyβ optical depths are several factors smaller than the Lyα optical

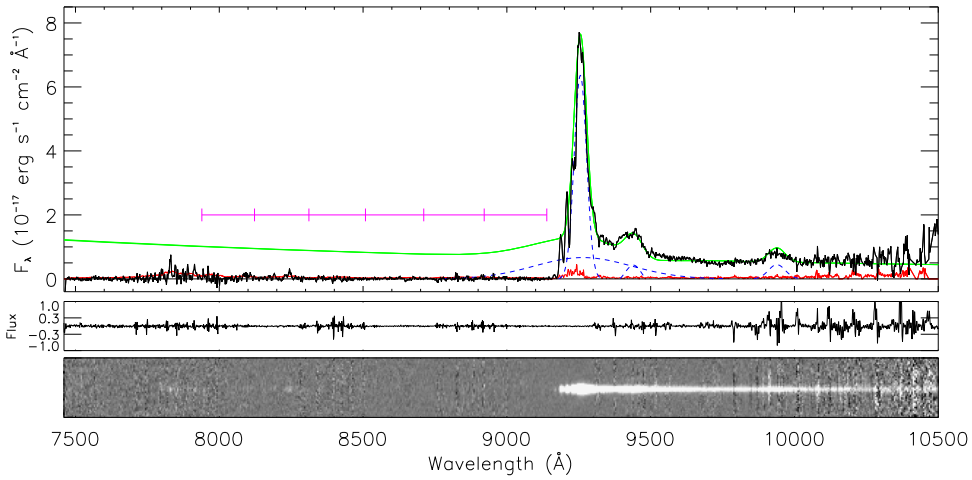

Figure 1. Subaru/FOCAS spectrum of PSO J006.1240+39.2219. In the upper panel, the green line is the best-fit continuum. The blue dashed lines are Gaussian fits to the emission lines. The redshift bins shown in purple horizontal line are used in analyzing the transmissions and optical depths. The red lines show the measured errors. The middle panel shows the sky spectrum in an arbitrary scale. The bottom panel shows the 2D spectrum of the QSO.

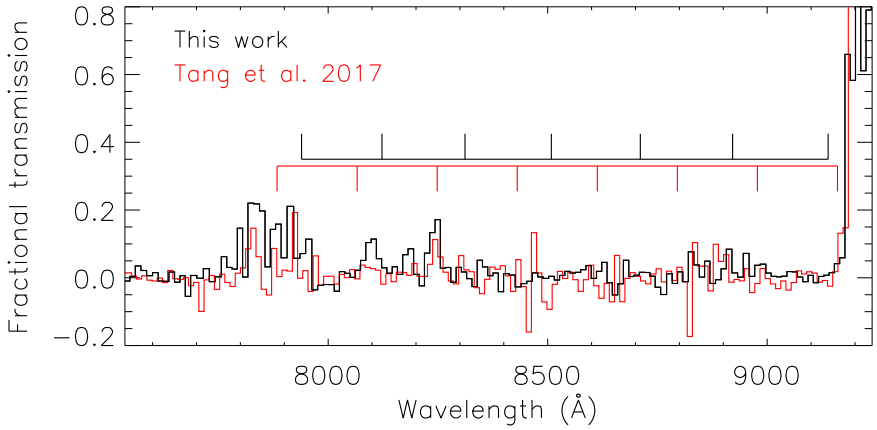

Figure 2. Fractional transmission spectra of this work (black) and the spectrum taken from Tang et al. (2017; red). Both are 8 pixel binned. The horizontal black and red rulers show the redshift bins used in this work and in Tang et al. (2017), respectively.

Table 2
The Lyα, N V λ1239,1243, and O I λ1304+ Si II λ1306 Emission Line Luminosities

Line	Luminosity (10^{44} erg s^{-1})
Lyα	17.75 ± 0.10
N V λ1239,1243	1.79 ± 0.06
O I λ1304+ Si II λ1306	1.54 ± 0.16

depths for the same hydrogen density, we calculate the weighted Lyβ transmissions and their effective optical depths ($\tau_\beta^{\rm eff}$). Following the discussion in Fan et al. (2006b), we first calculate the weighted Lyβ transmissions considering the foreground Lyα transmission at the corresponding observed wavelength. The foreground Lyα transmission is calculated using Equation (5) in Fan et al. (2006b), which is the best-fit power law for the optical depth at $z < 5.5$. Then, we convert the Lyβ transmissions into the effective optical depths by applying $\tau_\alpha/\tau_\beta = 2.25$ from Fan et al. (2006b). The result is shown in Table 3 and is plotted in Figures 3 and 4.

The uncertainty of the continuum and the noise level are taken into account in estimating the transmission error. When the flux detection is less than 2σ, we estimate the lower limit of the corresponding optical depth using 2σ error of the transmission.

We also measure the near zone radius ($R_{\rm p,NZ}$) of the QSO, using $R_{\rm p,NZ} = (D_{\rm Q} - D_{\rm GP})/(1+z_{\rm Q})$ (Fan et al. 2006b). We also correct the near zone radius for the luminosity difference, $R_{\rm NZ,corrected} = R_{\rm p,NZ} \times 10^{0.4(27+M_{1450})/3}$ (Carilli et al. 2010). $D_{\rm Q}$ and $D_{\rm GP}$ stand for the comoving distance of the QSO and

Table 3
The Transmissions and Optical Depths of PSO J006.1240+39.2219

Redshift	Wavelength range	Line	Transmission	τ_α
6.43	8921–9139	Lyα	0.011 ± 0.008	$4.6^{+1.5}_{-0.6}$
6.25	8711–8921	Lyα	0.013 ± 0.014	>4.6
6.08	8508–8711	Lyα	0.009 ± 0.013	>4.4
5.92	8312–8508	Lyα	0.002 ± 0.010	>4.6
5.76	8123–8312	Lyα	0.043 ± 0.018	$3.1^{+0.5}_{-0.4}$
5.61	7939–8123	Lyα	0.029 ± 0.024	$3.5^{+1.7}_{-0.6}$
6.45	7548–7732	Lyβ	0.031 ± 0.075	>6.0

Note. The transmission error and the optical depth error are in 2σ error.

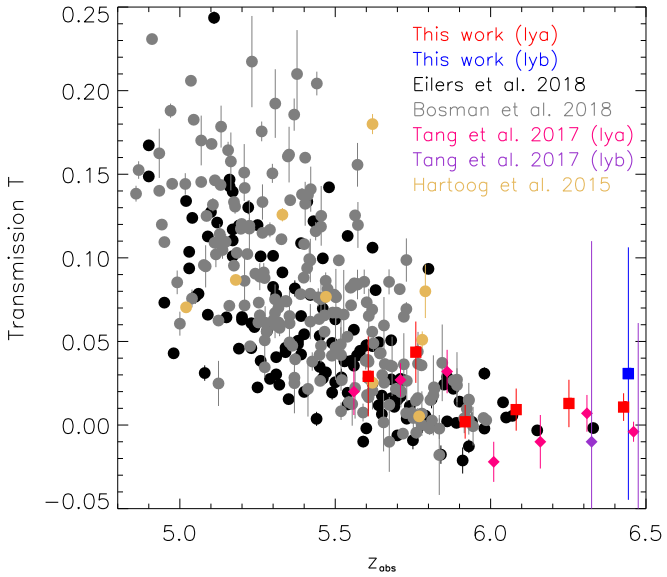

Figure 3. Lyα transmission vs. redshift. Red and blue squares with error bars are the Lyα and the effective Lyβ transmission in the spectrum of PSO J006.1240+39.2219, respectively. Pink and purple diamonds with error bars are the result of the same QSO from Tang et al. (2017). The rest of the data points are from previous studies (Hartoog et al. 2015; Bosman et al. 2018; Eilers et al. 2018) as indicated in the legend. Data points from Tang et al. (2017) are measured through the same LOS as this work, while Hartoog et al. (2015) is measured from a gamma-ray burst spectrum.

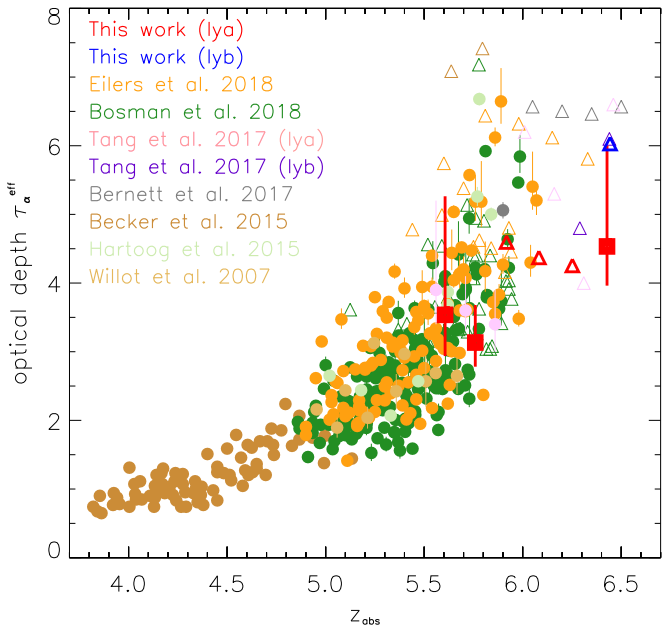

Figure 4. Effective Lyα optical depth as a function of redshift. Red (Lyα) and blue (Lyβ) squares with error bars or triangles are results from this work. The other data are taken from previous studies (Willott et al. 2007; Becker et al. 2015; Hartoog et al. 2015; Barnett et al. 2017; Tang et al. 2017; Bosman et al. 2018; Eilers et al. 2018). The triangles are the lower limit of the optical depth.

where the transmission first drops below 0.1, respectively. The near zone measurement is performed after smoothing the spectrum to $R \sim 2600$ with a boxcar function, following previous studies (e.g., Venemans et al. 2015; Eilers et al. 2017). We measure the values of $R_{\rm p,NZ}$ and $R_{\rm NZ,corrected}$ to be 4.19 ± 0.06 and 5.79 ± 0.09 (pMpc), respectively. The uncertainty of the near zone radius is $\Delta R_{\rm p,NZ} \sim 0.1$ (pMpc),

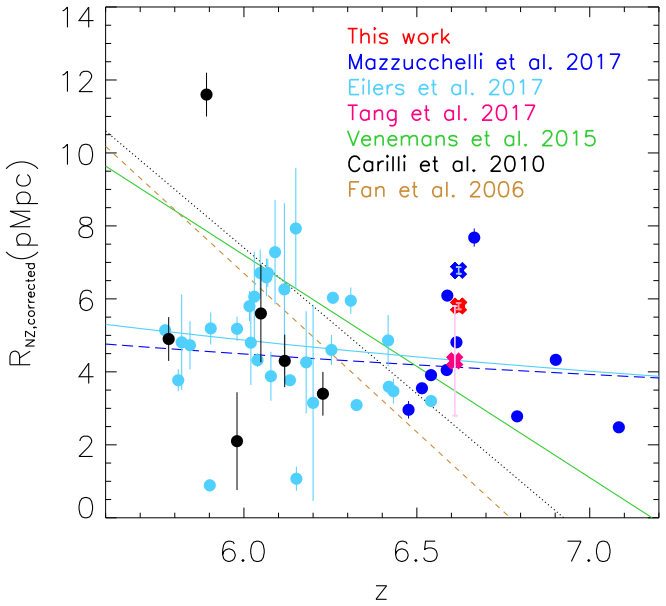

Figure 5. $R_{\rm NZ,corrected}$ of the QSOs. The red cross with an error bar is the result from this study. The brown dashed line is the fitted trend of $R_{\rm NZ,corrected}$ from Fan et al. (2006b). The green dash dot line is from Venemans et al. (2015). The black dots and dotted line are from Carilli et al. (2010). The cyan dots and solid line are from Eilers et al. (2017). The blue dots and long dash line are from Mazzucchelli et al. (2017). The pink and blue crosses with error bars are the $R_{\rm NZ,corrected}$ of the same QSO as this work measured by Tang et al. (2017) and Mazzucchelli et al. (2017).

due to the $z_{\rm [C\,II]}$ uncertainty of $\Delta z \sim 0.002$ (Carilli et al. 2010). These values are also shown in Table 1 and Figure 5 with comparison to previous literature results.

3.2. Dark Gap Statistics

With increasing redshift, absorption increases and it becomes more difficult to detect a flux. Hence, studying the epoch of reionization with the evolution of the average transmission may become less powerful. In contrast, measuring the separation between the sparse remaining flux becomes a better approach (Songaila & Cowie 2002; Becker et al. 2005; Fan et al. 2006b; Gallerani et al. 2006, 2008; Gnedin et al. 2017). With the medium-resolution spectrum, we can measure the dark gaps statistics for the first time at $z \sim 6.5$ with PSO J006.1240 +39.2219. The wavelengths with a detected flux in the spectrum could be seen as the relatively ionized regions where the light was not fully absorbed by the hydrogen. Namely, measuring the intervals of those peaks in the spectrum could be a probe of the occurrence frequency of the ionized regions. We follow the discussion in Section 5 of Songaila & Cowie (2002), measuring the width of the gap that is constructed by two adjacent $\tau \leqslant 2.5$ peaks, and then count the number of the gaps within the corresponding gap width bins in a redshift interval after smoothing the spectrum to $R \sim 2600$. We discard the peaks with widths narrower than the smoothed resolution, since the widths of the sky spikes at the observed frame are mostly narrower than the smoothed resolution. However, note that there could remain subsplitting of the opaque regions by wider skyline residuals. We also measure the gaps between the $\tau \leqslant 3.5$ peaks since the neutral fraction is higher at $z > 6$, and the $\tau > 2.5$ dark gap extends to the near zone and can only be the lower limit of the gap width in many cases (Fan et al. 2006b). The gap positions are shown in Figure 6. The

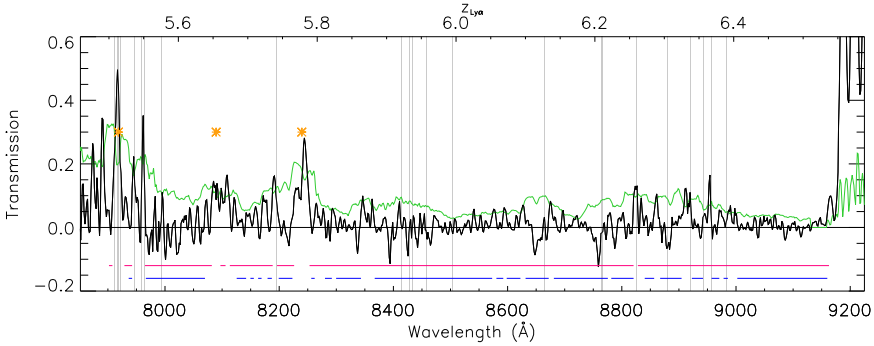

Figure 6. GP trough in the QSO spectrum. The spectrum was smoothed to $R \sim 2600$. The green lines are the 2σ spectral error. The orange asterisks show the positions of transmission spikes with more than 4 pixels with flux levels higher than the spectral error. The upper pink horizontal lines mark the $\tau > 2.5$ dark gaps. The lower blue horizontal lines mark the $\tau > 3.5$ dark gaps. The gray vertical lines show the positions of the pixels with strong skyline residuals.

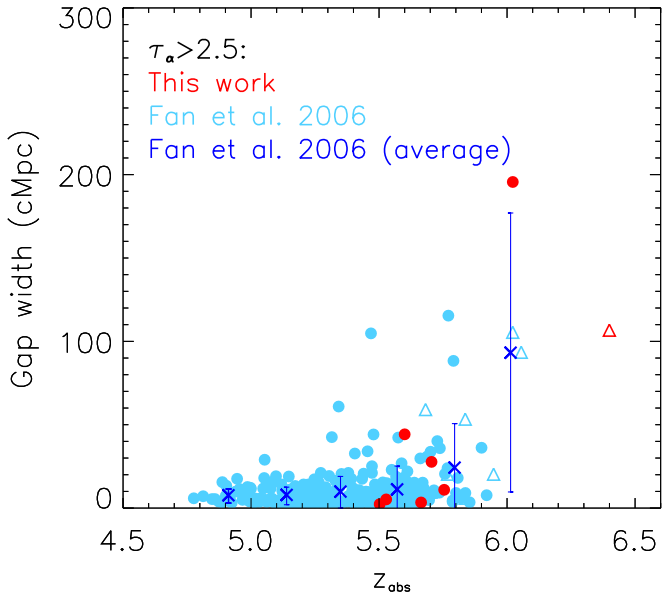

Figure 7. The $\tau > 2.5$ dark gap sizes and their corresponding redshift. The red dots and triangle are from this work. The light blue dots and triangles are the gap sizes taken from Fan et al. (2006b). Both red and light blue triangles represent the lower limit of the gap sizes. The deep blue crosses with error bars are the average gap sizes of the Fan et al. (2006b) data.

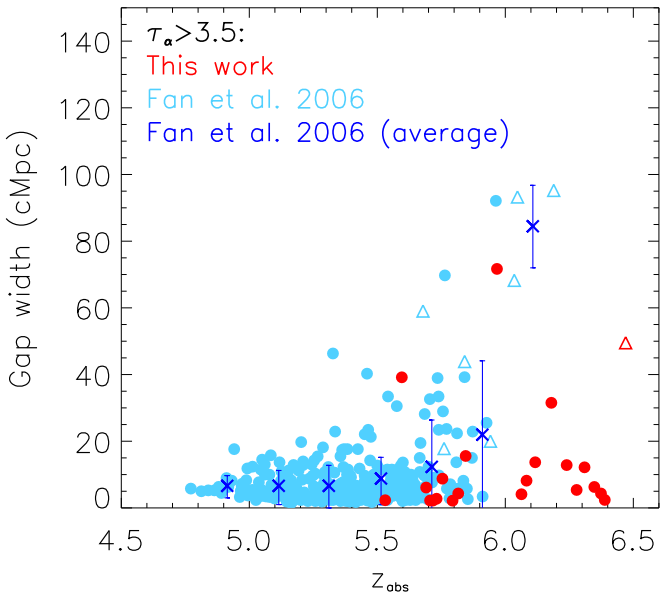

Figure 8. The $\tau > 3.5$ dark gap sizes and their corresponding redshift. All the legends are the same as Figure 7.

development of the $\tau > 2.5$ and the $\tau > 3.5$ gaps are shown in Figures 7 and 8, respectively, and the redshifts and widths of the gaps are shown in Table 4. The distributions of the $\tau > 2.5$ gaps at $5.5 < z < 6.0$ and $5.7 < z < 6.3$ are shown in Figure 9.

3.3. Dark Pixel

McGreer et al. (2011, 2015) proposed a model-independent method to constrain the upper limit of the volume-average neutral hydrogen fraction ($\langle x_{\rm H\,I}\rangle$) by directly measuring the covering fraction of the dark pixels. The dark pixels are the pixels in the spectrum with a flux under a given threshold, which was set to be 2σ rms noise (McGreer et al. 2011) or zero flux (McGreer et al. 2011, 2015). Two cases resulting in the dark pixels are discussed in McGreer et al. (2015): the pre-reionization neutral hydrogen in any physical region and the collapsed self-shielded region cause saturated absorption (the observed flux under the threshold); the ionized gas with sufficient optical depth result in fewer transmitted flux, which is below the detection limit. Compared to the neutral fraction derived from the IGM optical depth measurement, which requires assumptions on the intrinsic QSO continuum and uniform background, the dark pixels measurement provide a more robust result of the the neutral fraction.

The only assumption made in this measurement is that the dark pixels are distributed symmetrically around the threshold. In addition, it requires high S/N spectrum, in order to reduce the probability that a dark pixel counted as a bright pixel (pixel that is not dark) due to the noise.

We follow the procedure from McGreer et al. (2011). First, we divided the sky-masked spectrum into bins of pixels with a width of 3.3 pMpc (see the discussion in Section 3.3 of McGreer et al. 2011). Then we count the covering fraction of dark pixels where the flux $\leqslant 2\sigma$ (2σ threshold) and where the flux $\leqslant 0$ (zero flux threshold) in the same six 50 cMpc h^{-1} redshift bins as in Section 3.1. For the 2σ threshold, $\langle x_{\rm H\,I}\rangle$ are then derived by scaling the dark pixel covering fractions by a factor of 1.023 because 2.3% of the dark pixels are expected to scatter above the threshold, assuming Gaussian statistics. The

Table 4
The Redshifts and Widths of the $\tau_\alpha > 2.5$ and $\tau_\alpha > 3.5$ Dark Gaps in the Spectrum of PSO J006.1240+39.2219

Optical Depth	Redshift Range	$z_{\rm average}$	Gap Length (cMpc)
$\tau_\alpha > 2.5$	6.26–6.54	6.40	106.69
	5.79–6.26	6.02	195.60
	5.74–5.77	5.75	10.96
	5.67–5.74	5.71	27.70
	5.66–5.67	5.66	3.35
	5.55–5.65	5.60	44.24
	5.52–5.53	5.53	5.19
	5.50–5.50	5.50	2.32
$\tau_\alpha > 3.5$	6.41–6.53	6.47	49.52
	6.39–6.39	6.39	2.40
	6.37–6.38	6.37	4.33
	6.34–6.36	6.35	6.28
	6.29–6.32	6.31	12.18
	6.27–6.29	6.28	5.39
	6.22–6.26	6.24	12.85
	6.14–6.22	6.18	31.52
	6.10–6.13	6.11	13.69
	6.07–6.09	6.08	8.17
	6.06–6.07	6.06	4.10
	5.88–6.05	5.97	71.69
	5.83–5.86	5.85	15.58
	5.81–5.82	5.82	4.33
	5.79–5.80	5.79	2.17
	5.74–5.76	5.75	8.77
	5.73–5.73	5.73	2.75
	5.71–5.72	5.72	2.21
	5.70–5.71	5.71	2.21
	5.68–5.70	5.69	6.11
	5.55–5.64	5.60	39.17
	5.53–5.53	5.53	2.30

uncertainties of the $\langle x_{\rm H\,I}\rangle$ are calculated after scaling. In contrast to the way the uncertainties are calculated in McGreer et al. (2011, 2015), where the jackknife method was adopted for the multi sight lines, we simply calculate the uncertainties by taking the square root of the fractions for a single sight line. For the zero flux threshold, the scaling factor is adjusted to be 2, because the dark pixels under this threshold are expected to scatter equally around zero. The uncertainties for the zero flux threshold are calculated in the same manner as for the 2σ threshold. Results are shown in Figure 10 and Table 5. The $\langle x_{\rm H\,I}\rangle$ measured using both criteria shows a growing trend toward high redshift, but the result from the 2σ threshold shows higher $\langle x_{\rm H\,I}\rangle$. This difference is expected since at such redshifts, the transmitted fluxes approach zero. Hence, using the zero flux threshold is more appropriate because it could reveal subtler fractional changes than using the 2σ threshold.

4. Discussion

With the medium-resolution spectrum of the target, we perform three different absorption tests to understand cosmic reionization. We extend the measurement of the GP transmission, the dark gap, and dark pixel statistics to $z \sim 6.5$, where constraints are still poor. The results are consistent with the sudden change around $5.8 \leqslant z \leqslant 6.1$, suggesting the end stage of the reionization epoch at the redshift interval, which is also consistent with previous studies (Fan et al. 2006b; Bosman et al. 2018; Eilers et al. 2018). Our measurements at $z > 6.18$ also indicate a continuing trend of increasing neutral fractions toward higher redshifts. However, we find a subtle difference in our results.

Table 5
The Dark Pixel Fractions in Each Redshift Bin Measured with 2σ Criteria with Zero Flux Criteria

Redshift	Wavelength Range (Å)	Line	$\langle x_{\rm H\,I}\rangle$ (2σ)	$\langle x_{\rm H\,I}\rangle$ (Zero Flux)
6.43	8921–9139	Lyα	0.94 ± 0.08	0.78 ± 0.07
6.25	8711–8921	Lyα	0.96 ± 0.08	0.81 ± 0.08
6.08	8508–8711	Lyα	0.94 ± 0.08	0.78 ± 0.08
5.92	8312–8508	Lyα	1.00 ± 0.09	0.91 ± 0.09
5.76	8123–8312	Lyα	0.94 ± 0.09	0.56 ± 0.07
5.61	7939–8123	Lyα	0.94 ± 0.09	0.72 ± 0.08
6.45	7548–7732	Lyβ	0.98 ± 0.09	0.97 ± 0.09

For the IGM transmission measurement, the factors affecting the measurement come from the different ways to extrapolate the intrinsic continuum to the blueward of Lyα emission, the LOS variance, and the data quality. First, there are two main ways to extrapolate the continuum to the blue of the Lyα emission line, using the power-law continuum (or power-law plus Lyα and $N_{\rm V}$ λ1239,1243 emissions) (Fan et al. 2006b; Becker et al. 2015; Barnett et al. 2017; Bosman et al. 2018) or using the principal component analysis (PCA; Mazzucchelli et al. 2017; Eilers et al. 2018). PCA tends to predict higher continuum levels (Eilers et al. 2018), thus the transmissions measured by PCA would be lower.

Eilers et al. (2018) and Fan et al. (2006b) measured the same sight lines but found the median transmission difference of -0.023. Because these measurements are in the same sight line, the sources of the difference could be different observations, different data reduction, and a different continuum estimation. While Eilers et al. (2018) used PCA to estimate the continua, Fan et al. (2006b) assumed a power-law continua. Besides, the mean transmission in Eilers et al. (2018) is $\sim$0.02 lower than that measured by Bosman et al. (2018) using a power-law continuum at $5 < z < 6$ but through different LOSs. However, because these measurements are through different sight lines, it is unclear how much of the difference is due to the systematics and how much is from the inhomogeneity of the reionization. Compared with our measurements, at $z > 6$, Eilers et al. (2018) measured $T \approx 0$ (Figure 3) using the PCA continuum, while the transmission in this work is $\approx 0.011 \pm 0.009$, which is higher but still consistent within 2σ, in a different sight line. Because these QSOs are at different sight lines, the difference of 0.011 could be due to the inhomogeneity in reionization. In addition, the data quality and data analysis are crucial for the transmission measurement at high z as well. At $z > 6$, the GP absorption can be easily saturated due to the highly opaque IGM. Because of this, only a few faint transmission spikes can be observed. However, this wavelength window is overlapped with sky emissions. Compared with Tang et al. (2017), because we have a higher S/N and a longer exposure time spectrum in this work, the sky contamination is weaker and the transmitted spikes are seen more clearly (Figure 2). Instead of masking the sky, Tang et al. (2017) measure the squared-spectrum-error-weighted transmission to reduce the effect of the sky. However, their result is still suffering from the oversubtracted sky. Nevertheless, our result is consistent within 2σ. The near zone region, measured from the transmission, aside from the diverse property between

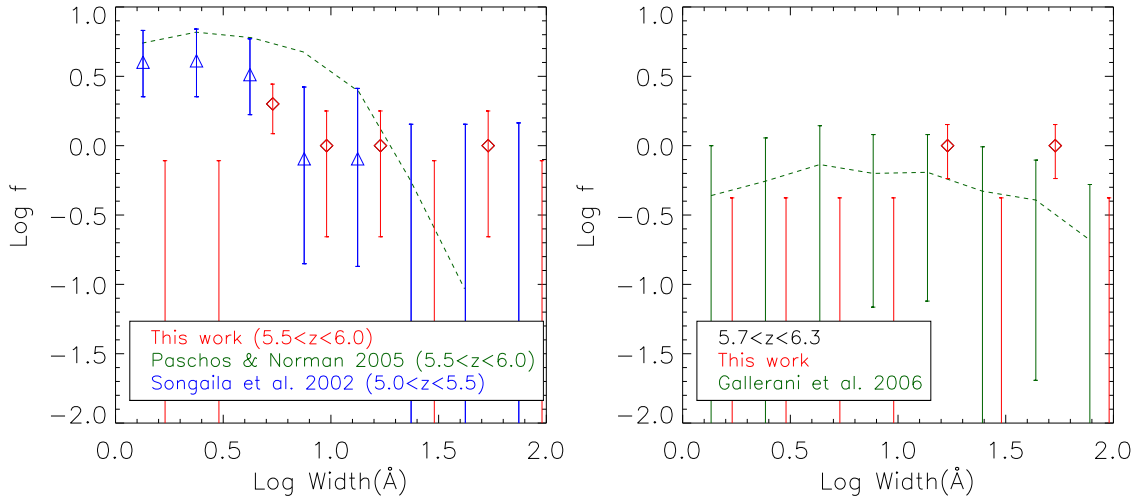

Figure 9. Number of dark gaps ($\tau > 2.5$) per unit redshift vs. the gap width. Left: red diamonds are the distribution of gaps from this work ($5.5 < z < 6.0$). Blue triangles are the observational result ($5.0 < z < 5.5$) taken from Songaila & Cowie (2002). The green dashed line is the simulation of Paschos & Norman (2005). Right: red diamonds are the distribution of gaps from this work ($5.7 < z < 6.3$). The green dashed line are the simulation of Gallerani et al. (2006).

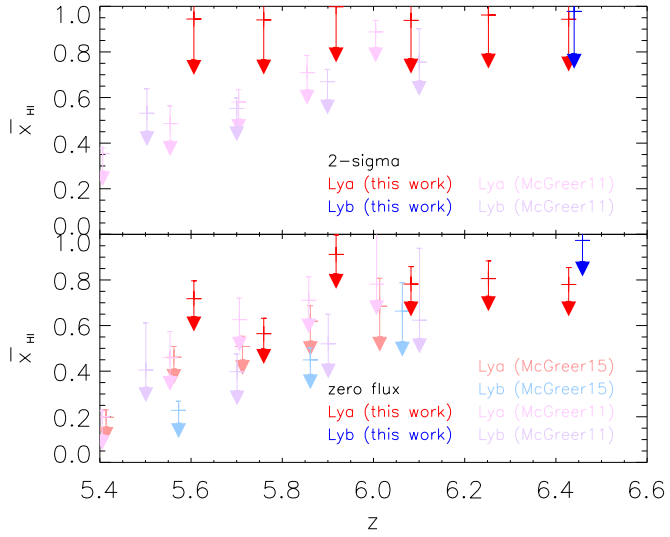

Figure 10. Upper limit of $\langle x_{\rm H\,I} \rangle$. The upper panel shows the test using the 2σ threshold. The red and blue arrows are the results from this work. The length of arrows represents the statistical error. The pink and purple arrows are taken from McGreer et al. (2011). The lower panel shows the test using the zero flux threshold. The red and blue arrows are from this work. The pink and purple arrows are from McGreer et al. (2011). The faint red and blue arrows are from the data of McGreer et al. (2015).

individual QSOs, also has an LOS difference and a difference between different data quality and analyses. The $R_{\rm NZ,corrected}$ of this QSO is within the scatter of other $z \sim 6.5$ QSOs. When comparing $R_{\rm NZ,corrected}$ of the same QSO measured in different studies, the $R_{\rm NZ,corrected}$ we measured is 5.79 ± 0.09 *p*Mpc, which agrees with the previous measurement of 4.3 ± 1.5 *p*Mpc by Tang et al. (2017) within the uncertainty. However, it is in disagreement with 6.78 ± 0.09 *p*Mpc by Mazzucchelli et al. (2017). We suspect the disagreement is due to the different observations and data analyses; the exposure times were 30 and 83.3 minutes in Mazzucchelli et al. (2017) and in Tang et al. (2017), while our spectrum was measured with 7.5 hr of exposure time. The scarcely remaining flux at such wavelengths could lead to the larger uncertainty on the measurements. Moreover, Mazzucchelli et al. (2017) used the correction function derived by Eilers et al. (2017) for higher-redshift QSOs, which is $R_{\rm NZ,corrected} = R_{\rm p,NZ} \times 10^{0.4(27+M_{1450})/2.35}$. The scale factor is 1.094 times larger than ours, resulting in a closer value of 6.33 *p*Mpc if we multiply our result by 1.094. In addition, the continuum estimation methods were largely different. Mazzucchelli et al. (2017) performed the continuum fitting using PCA, the transmission profile at the near zone region depends on how well PCA can reconstruct the intrinsic spectrum. To overcome the shortage of the transmission measurement, we take advantage of the high resolution and high S/N rate spectrum to try two additional methods.

In the dark gap distribution, the gap width development of both the $\tau > 2.5$ gaps and $\tau > 3.5$ gaps in our spectrum follow a similar rising trend as in Fan et al. (2006b) at $z \lesssim 6$. However, at $z > 6$, the sizes of the $\tau > 3.5$ gaps decrease predominantly due to the presence of the skyline residuals and the near zone region of the QSO. To be consistent with previous studies (Songaila & Cowie 2002; Fan et al. 2006b), we do not attempt to eliminate the skyline residuals. We caution that the dark gap could be subsplit into smaller gaps by the skyline residuals, especially for the $\tau > 3.5$ gaps. In Figure 9, we measure the $\tau > 2.5$ dark gap distribution at $5.5 < z < 6.0$ and $5.7 < z < 6.3$ in order to compare it with previous observations (Songaila & Cowie 2002) and simulations (Paschos & Norman 2005; Gallerani et al. 2006). At $5.5 < z < 6.0$, we compare our result to the simulation from Paschos & Norman (2005) at the same redshift range but with a finer resolution ($R = 5300$), and to the observation from Songaila & Cowie (2002) at the same smoothed resolution ($R = 2600$) but at lower redshift ($5.5 < z < 6.0$). While the gap widths in Songaila & Cowie (2002) are mostly shorter than 18 Å, the widths measured in this work extends to ∼56 Å. The redshift evolution of the gap width is clearly seen. When compared with Paschos & Norman (2005), our result is inconsistent with their simulation. The limited box size (6.8 cMpc) in their simulation was pointed out by Gallerani et al. (2006). The resolution difference causes the discrepancy as well. As shown in Paschos & Norman (2005), the fraction of the narrower gaps is higher in simulations when the resolution is higher. At $5.7 < z < 6.3$, the resolution of the simulation performed by Gallerani et al. (2006) had been smoothed to the

resolution similar to the spectral resolution in Songaila & Cowie (2002). Although our result is consistent within 1σ with simulations, the distribution measured through only a single LOS is insufficient. Observations of more dark gaps at $z > 5.5$ are required to draw the final conclusion.

For the dark pixel fraction, we extend the measurement to $z \sim 6.5$ with this single target. Simply comparing our result to the statistical result shown in McGreer et al. (2011, 2015), the measurement using the 2σ threshold is much higher than that from using the negative pixel threshold. The 2σ threshold method is sensitive to how accurate the per pixel noise can be measured. In Figure 10's bottom panel (the zero flux threshold), we measure the upper limit of $\langle x_{\rm H\,I}\rangle \sim 0.8$ at $z \sim 5.8$, which is larger than the measurement of McGreer et al. (2015). This again suggests the requirement for more high-redshift QSO spectra, since there is a wide LOS variance at these redshifts.

5. Summary

We obtained a deep, medium-resolution optical spectrum of the QSO PSO J006.1240+39.2219, at $z = 6.62$ with the Subaru 8 m telescope. We measure the line luminosity of Lyα as $17.75 \pm 0.10 \times 10^{44}$ erg s^{-1}, N V λ1239,1243 as $1.79 \pm 0.06 \times 10^{44}$ erg s^{-1}, and the O I λ1304+ Si II λ1306 as $1.54 \pm 0.16 \times 10^{44}$ erg s^{-1}. We found a slightly smaller τ than previous studies at $z > 6$. However, τ is still increasing with increasing redshifts. The redshift of the sudden change in opacity is consistent with literature, which is around $z \sim 5.8$. The normalized $R_{\rm NZ,corrected}$ is 5.62 ± 0.09 pMpc, which is consistent with decreasing sizes at higher z. We also investigate the distribution of the dark gaps in the spectrum, which also shows a significant increase of the gap widths at $z > 6$. Furthermore, we extend the dark pixel measurements to $z > 6$. Using the zero flux threshold, the measured upper limit at $z < 5.8$ is $\langle x_{\rm H\,I}\rangle \sim 0.5$, while the upper limit is $\langle x_{\rm H\,I}\rangle \sim 0.8$ at $z > 5.8$.

We thank the anonymous referee for many helpful suggestions. T.G. acknowledges the support by the Ministry of Science and Technology of Taiwan (MOST) through grant 105-2112-M-007-003-MY3 and 108-2628-M-007-004-MY3. T.Y.L. acknowledges the support by the MOST through grant 107-2813-C-007-104-M. A.Y.L.O. and T.H. are supported by the Center for Informatics and Computation in Astronomy (CICA) at National Tsing Hua University (NTHU) through a grant from the Ministry of Education of the Republic of China (Taiwan). A.Y.L.O.'s visit to NTHU is hosted by Professor Albert Kong and supported by the MOST through grant 105-2119-M-007-028-MY3.

ORCID iDs

Ting-Yi Lu https://orcid.org/0000-0002-4965-6524
Tomotsugu Goto https://orcid.org/0000-0002-6821-8669
Ji-Jia Tang https://orcid.org/0000-0002-1860-0886
Tetsuya Hashimoto https://orcid.org/0000-0001-7228-1428
Chia-Ying Chiang https://orcid.org/0000-0002-9630-4003
Seong Jin Kim https://orcid.org/0000-0001-9970-8145
Simon C.-C. Ho https://orcid.org/0000-0002-8560-3497
Ting-Wen Wang https://orcid.org/0000-0002-1151-7094
Alvina Y. L. On https://orcid.org/0000-0003-4479-4415
Daryl Joe D. Santos https://orcid.org/0000-0002-5687-0609

References

Bañados, E., Venemans, B. P., Mazzucchelli, C., et al. 2018, Natur, 553, 473
Barkana, R., & Loeb, A. 2001, PhR, 349, 125
Barnett, R., Warren, S. J., Becker, G. D., et al. 2017, A&A, 601, A16
Becker, G. D., Bolton, J. S., Madau, P., et al. 2015, MNRAS, 447, 3402
Becker, G. D., Sargent, W. L. W., & Rauch, M. 2005, in IAU Coll. 199, Probing Galaxies Through Quasar Absorption Lines, ed. P. R. Williams, C.-G. Chu, & B. Menard (Cambridge: Cambridge Univ. Press), 357
Becker, R. H., Fan, X., White, R. L., et al. 2001, AJ, 122, 2850
Bolton, J. S., Haehnelt, M. G., Warren, S. J., et al. 2011, MNRAS, 416, L70
Bosman, S. E. I., Fan, X., Jiang, L., et al. 2018, MNRAS, 479, 1055
Carilli, C. L., Wang, R., Fan, X., et al. 2010, ApJ, 714, 834
Croft, R. A. C., & Gaztañaga, E. 1998, ApJ, 495, 554
Eilers, A.-C., Davies, F. B., & Hennawi, J. F. 2018, ApJ, 864, 53
Eilers, A.-C., Davies, F. B., Hennawi, J. F., et al. 2017, ApJ, 840, 24
Fan, X., Carilli, C. L., & Keating, B. 2006a, ARA&A, 44, 415
Fan, X., Narayanan, V. K., Strauss, M. A., et al. 2002, AJ, 123, 1247
Fan, X., Strauss, M. A., Becker, R. H., et al. 2006b, AJ, 132, 117
Gallerani, S., Choudhury, T. R., & Ferrara, A. 2006, MNRAS, 370, 1401
Gallerani, S., Ferrara, A., Fan, X., et al. 2008, MNRAS, 386, 359
Gnedin, N. Y., Becker, G. D., & Fan, X. 2017, ApJ, 841, 26
Goto, T., Utsumi, Y., Hattori, T., et al. 2011, MNRAS, 415, L1
Gunn, J. E., & Peterson, B. A. 1965, ApJ, 142, 1633
Hartoog, O. E., Malesani, D., Fynbo, J. P. U., et al. 2015, A&A, 580, A139
Inayoshi, K., Visbal, E., & Haiman, Z. 2019, arXiv:1911.05791
Kashikawa, N., Aoki, K., Asai, R., et al. 2002, PASJ, 54, 819
Keating, L. C., Kulkarni, G., Haehnelt, M. G., et al. 2019, arXiv:1912.05582
Keating, L. C., Weinberger, L. H., Kulkarni, G., et al. 2020, MNRAS, 491, 1736
Loeb, A., & Barkana, R. 2001, ARA&A, 39, 19
Mazzucchelli, C., Bañados, E., Venemans, B. P., et al. 2017, ApJ, 849, 91
McGreer, I. D., Mesinger, A., & D'Odorico, V. 2015, MNRAS, 447, 499
McGreer, I. D., Mesinger, A., & Fan, X. 2011, MNRAS, 415, 3237
Mortlock, D. 2016, in Understanding the Epoch of Cosmic Reionization, Challenges and Progress, ed. A. Mesinger (Cham: Springer), 187
Nasir, F., & D'Aloisio, A. 2019, arXiv:1910.03570
Planck Collaboration, Aghanim, N., Akrami, Y., et al. 2018, arXiv:1807.06209
Paschos, P., & Norman, M. L. 2005, ApJ, 631, 59
Songaila, A. 2004, AJ, 127, 2598
Songaila, A., & Cowie, L. L. 2002, AJ, 123, 2183
Tang, J.-J., Goto, T., Ohyama, Y., et al. 2017, MNRAS, 466, 4568
Tang, J.-J., Goto, T., Ohyama, Y., et al. 2019, MNRAS, 484, 2575
Venemans, B. P., Bañados, E., Decarli, R., et al. 2015, ApJL, 801, L11
Willott, C. J., Delorme, P., Omont, A., et al. 2007, AJ, 134, 2435